Development of an Earth Smallsat Flight Test to Demonstrate Viability of Mars Aerocapture

Michael S. Werner[1], Bryce A. Woollard[2], Anirudh Tadanki[3] and Swapnil R. Pujari[4]
Space Systems Design Laboratory, Georgia Institute of Technology, Atlanta, GA, 30318

Robert D. Braun[5]
University of Colorado Boulder, Boulder, CO, 80309

and

Robert E. Lock[6], Adam P. Nelessen[7] and Ryan C. Woolley[8]
Jet Propulsion Laboratory, California Institute of Technology, La Cañada Flintridge, CA, 91109

A smallsat mission concept is developed to demonstrate the feasibility of an aerocapture system at Earth. The proposed mission utilizes aerocapture to transfer from a GTO rideshare trajectory to a LEO. Single-event drag modulation is used as a simple means of achieving the control required during the maneuver. Numeric trajectory simulations and Monte Carlo uncertainty analyses are performed to show the robustness of the system to day-of-flight environments and uncertainties. Similar investigations are performed at Mars to show the relevance of the proposed mission concept to potential future applications. The spacecraft design consists of a 24.9 kg vehicle with an attached rigid drag skirt, and features commercially-available hardware to enable flight system construction at a university scale. Results indicate that the proposed design is capable of targeting the desired final orbit, surviving the aerothermodynamic and deceleration environments produced during aerocapture, and downlinking relevant data following the maneuver.

Nomenclature

A	=	aerodynamic reference area
C_D	=	drag coefficient
$C_{m,\alpha}$	=	pitching moment static stability derivative
m	=	mass
$\hat{x}$	=	static margin
α	=	angle of attack
β	=	ballistic coefficient
ΔV	=	change in velocity
σ	=	standard deviation

---

[1] Graduate Research Assistant, School of Aerospace Engineering, 270 Ferst Drive, AIAA Non-Member.

[2] Graduate Research Assistant, School of Aerospace Engineering, 270 Ferst Drive, AIAA Non-Member.

[3] Undergraduate Research Assistant, School of Aerospace Engineering, 270 Ferst Drive, AIAA Non-Member.

[4] Graduate Research Assistant, School of Aerospace Engineering, 270 Ferst Drive, AIAA Student Member.

[5] Dean, College of Engineering and Applied Science, 1111 Engineering Drive, AIAA Fellow.

[6] Orbiter Development Manager, Mars Program Formulation Office, 4800 Oak Grove Dr. M/S 301-165, AIAA Non-Member.

[7] Systems Engineer, Project Systems Engineering and Formulation, 4800 Oak Grove Dr. M/S 301-165, AIAA Non-Member.

[8] Mission Design Engineer, Inner Planets Mission Design Group, 4800 Oak Grove Dr. M/S 301-121, AIAA Non-Member.

1

American Institute of Aeronautics and Astronautics

I. Introduction

FUTURE space exploration missions will require the delivery of increasingly massive payloads to different planetary targets. As payload mass continues to increase and more challenging destinations are selected, innovative methods of orbital insertion will be required. For missions to planets with an appreciable atmosphere, aeroassist technologies are promising alternatives to traditional methods. These technologies involve the use of atmospheric forces as a means of deceleration, which may result in mass and cost savings when compared to propulsive insertion.

One such technology is aerocapture. Aerocapture is an orbital maneuver that utilizes the drag generated during atmospheric entry to capture directly into a specific orbit, as shown in Fig. 1. Aerocapture has long been recognized as a technology with a number of potential benefits for space missions[1]. The use of atmospheric drag as a means of deceleration drastically reduces the fuel requirements of many orbital missions, and the single atmospheric pass required for aerocapture can offer reductions in mission time and cost when compared to aerobraking. As a result, aerocapture can improve the size of payloads delivered to specific orbits, and enable other orbits altogether[2].
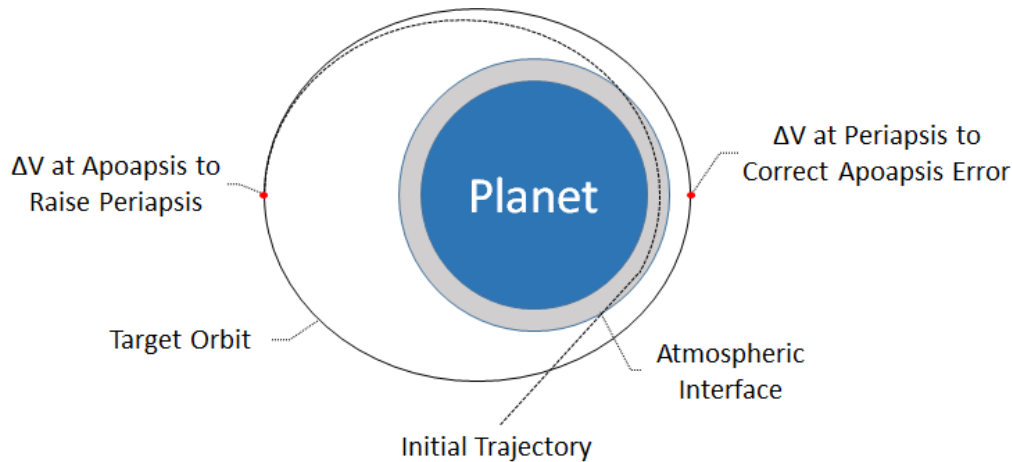

Figure 1. Sample aerocapture mission structure.

Numerous methods of aerocapture have been analytically shown as viable for a range of planetary missions[3-5]. Despite this and the potential benefits of utilizing aerocapture, the technique has not yet been used on a flight mission, with the lack of an integrated flight system demonstration often cited as a rationale. To this end, different flight tests and missions featuring aerocapture have been proposed in the past, although these proposals have been unsuccessful[6]. Simplifying different aspects of the aerocapture mission might yield a flight test that is more likely to be selected by virtue of being less expensive and easier to implement.

Recent research has focused on drag modulation as a means of simplifying traditionally complex control requirements. Drag modulation systems utilize changes in a vehicle's drag area, C_DA, during flight to affect control over the vehicle's β and therefore its energy depletion rate and final trajectory:

$$\beta = \frac{m}{C_DA} \qquad (1)$$

Drag modulation may be especially suited for aerocapture, as landing range is not considered – only the energy of the system must be controlled to achieve a desired final orbit. Compared to traditional bank-to-steer lifting methods, drag modulation techniques may greatly reduce the intricacy of an aerocapture flight system by eliminating the need for an onboard propulsive reaction control system and asymmetric flight conditions.

Drag modulation systems have been paired with aeroassist mission concepts before. McRonald examined the use of trailing inflatable ballutes for planetary entry applications at Mars, Venus, Earth, Titan, and other targets; he noted that releasing the ballute at the appropriate point in an atmospheric trajectory can result in an entry corridor for aerocapture[7]. Jettisoning an attached drag device in this manner accomplishes a single, discrete-event drag modulation, in which a vehicle's β is modified at one discrete point during its trajectory. Other studies have investigated the validity of similar aerocapture mission profiles featuring ballutes[3, 8]. Recently, Putnam et al. examined the performance of continuous and discrete-event drag modulation systems for aerocapture at different celestial targets. For missions to

2
American Institute of Aeronautics and Astronautics

Mars, Titan, and Earth, they showed the existence of feasible entry corridors that are robust to day-of-flight uncertainties[9, 10].

This investigation is focused on the development of a comprehensive smallsat mission concept that will demonstrate the feasibility of a drag-modulated aerocapture system at Earth. A successful mission would be a simple and inexpensive way to show that drag modulation-based aerocapture can be used as an effective means of orbit insertion at Earth, Mars, and other atmospheric worlds, with scalable applications to both small and large spacecraft. The remainder of this paper will be focused on the results of this mission concept study and will discuss each different aspect of the proposed concept. Section 2 lists the mission success criteria and examines the mission timeline in depth. Section 3 outlines the methodology used to analyze the proposed trajectory, and showcases the results of an end-to-end uncertainty analysis. Section 4 goes into detail about the mechanical design of the spacecraft. Section 5 contains a systems-level analysis of the flight system.

II. Mission Design

The main objective for this mission is to successfully perform an aerocapture maneuver in order to affect a significant change in the spacecraft's orbit. The prevalence of smallsat and CubeSat missions in recent years have shown that minimalistic designs can deliver quality results at a scale conducive to university teams; this type of philosophy was prioritized during mission design.

Specific, high-level mission goals include receiving a nominal ΔV of 2 km/s from a drag-modulated aerocapture maneuver, performing a propulsive maneuver to raise the perigee of the resulting orbit out of Earth's atmosphere, and returning data such that the performance of the aerocapture maneuver can be characterized post-hoc. The specific data products returned are tied to detailed success criteria, shown below in Table 1.

Table 1. Mission success criteria.

Success Category	Criteria
Threshold mission success	Spacecraft detected within acceptable range of target final orbit
Baseline mission success	1hz 6-DOF inertial measurement unit (IMU) and thermal data from aerocapture and propulsive maneuvers returned by spacecraft
Bonus mission success	Higher rate IMU and thermal data from aerocapture and propulsive maneuvers returned by spacecraft

The baseline architecture for this mission drew inspiration from the Aerocapture Flight Test Experiment, a prior flight test proposal outlined by Hall in Ref. 6. A timeline of the selected architecture is shown in Fig. 2. Aerocapture normally involves transfer from a hyperbolic orbit to an elliptical orbit around a planetary target. To demonstrate a roughly analogous transfer at Earth, a geosynchronous transfer orbit (GTO) was selected as the spacecraft's high energy initial orbit. Due to the prevalence of communication satellite launches to GTO, this starting orbit enables the smallsat to fly as a secondary payload, which greatly reduces cost when compared to a demonstration requiring a dedicated launch vehicle.
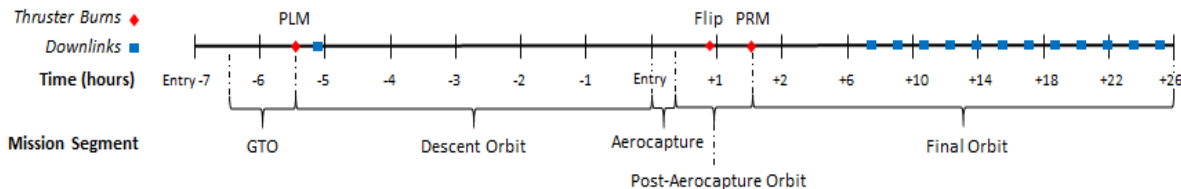

Figure 2. Nominal mission timeline.

The baseline rideshare option for this demonstration is provided by Space Systems Loral, who offer secondary payload opportunities to a GTO with an apogee altitude of 35,786 km and a perigee altitude of 185 km. During the rideshare, the host spacecraft will provide power and updated attitude knowledge to the smallsat. It is also desirable that the smallsat be mounted to the host in such a way that an initial spin rate can be imparted before separation from the host, to provide spin stabilization throughout the smallsat's trajectory. Means of achieving this initial spin rate will require further investigation. Separation from the host will occur one hour prior to apogee.

American Institute of Aeronautics and Astronautics

Once the smallsat reaches GTO apogee, it will perform a small propulsive maneuver to lower its perigee into Earth's atmosphere. This perigee-lower maneuver (PLM) is a byproduct of transferring from one elliptical orbit to another, and is not normally required for aerocapture. The PLM will use a predefined amount of fuel to generate a ΔV of 13.2 m/s and will result in a nominal altitude at perigee of 60 km. Following the maneuver, a data downlink will then occur to relay information about the vehicle's health and current orbit. From here, the spacecraft will coast for approximately 5 hours until it reaches Earth's atmosphere.

Once the atmosphere has been reached, single-event drag modulation flight control will be employed to target the desired post-maneuver orbit. A diagram of this technique is shown in Fig. 3. The spacecraft will enter the atmosphere traveling approximately 10.3 km/s, with a β that has been lowered via an attached rigid drag skirt to $\beta_1 = 66.4$ kg/m^2. During atmospheric flight, accelerometer data will be used by the flight computer to determine when to jettison the drag skirt such that the target orbit is achieved. Upon drag skirt jettison, the spacecraft will be flying with a $\beta_2 = 302.0$ kg/m^2 and will experience greatly reduced deceleration as a result. The smallsat will then exit the atmosphere traveling approximately 8.3 km/s, resulting in an orbit with an apogee altitude of 1,760 km and a perigee altitude of 60 km.
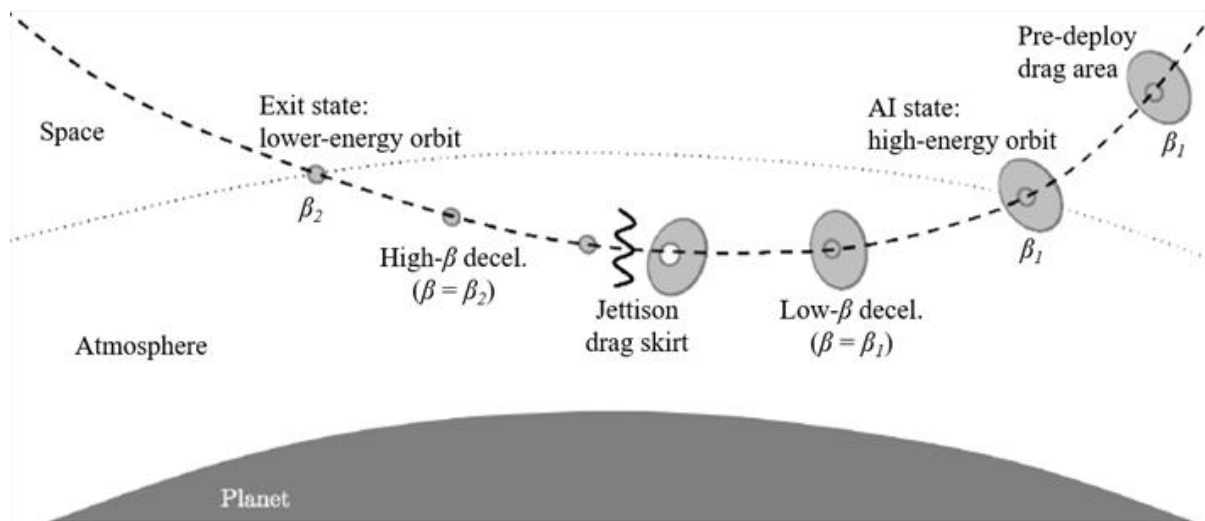

Figure 3. Single-event drag modulation diagram[10].

Following atmospheric exit, the spacecraft will utilize the attitude control capabilities of its thrusters to rotate 180 degrees, reorienting its propulsion system for a second burn. Upon reaching apogee of the post-atmospheric orbit approximately 30 minutes after this reorientation, a second propulsive maneuver will be performed to raise the spacecraft's perigee out of Earth's atmosphere. This perigee-raise maneuver (PRM) will require a ΔV of 33.8 m/s and will result in a final orbit with an apogee altitude of 1,760 km and a perigee altitude of 180 km. Once this orbit has been reached, data downlink will begin. The spacecraft will then be left to naturally deorbit within the 25 year smallsat deorbit requirement.

III.   Trajectory and Uncertainty Analysis

A. Trajectory Modeling

The smallsat will experience its most extreme conditions during the atmospheric portion of its trajectory. A numeric trajectory simulation was used in order to analyze the vehicle's performance during this phase. This simulation uses a fourth-order Runge-Kutta scheme to numerically integrate the 3-DOF equations of motion. The Earth was modeled as a sphere with inverse square gravity and J2 perturbations. Heating at the stagnation point was approximated using the Sutton-Graves relation, and radiative heating was not modeled. Use of this simulation enabled quick analysis of peak deceleration, convective heat rates, and post-aerocapture orbits for potential trajectories.

Initial conditions for this simulation consist of the vehicle's state at atmospheric interface. This state for the

Table 2.   Trajectory simulation initial conditions.

Parameter	Value
Inertial velocity magnitude	10.3 km/s
Inertial flight path angle	-5.04°
Inertial azimuth	90°
Altitude	125 km
Latitude	0°
Longitude	169°

4

American Institute of Aeronautics and Astronautics

spacecraft's nominal trajectory is shown in Table 2. In order to target the desired post-aerocapture orbit, the drag skirt jettison event is controlled through the use of a real-time numeric predictor-corrector guidance algorithm. This algorithm was developed in Ref. 9 and utilizes accelerometer data from the navigation system to determine the appropriate time to jettison the drag skirt. The algorithm also incorporates a constant-bias atmospheric density corrector to improve the vehicle's response to day-of-flight uncertainties in the atmosphere. The flight computer was modeled with a relatively conservative guidance execution rate of 0.5 hz, due to the computational intensity of the numeric predictor-corrector algorithm and the limited processing power of typical commercially-available smallsat flight computers.

Figure 4 shows simulation results for the spacecraft's nominal trajectory. During atmospheric flight, the vehicle reaches a minimum altitude of approximately 70 km. Once the flight computer determines enough energy has been lost, the external drag skirt is jettisoned. As a result, an instantaneous increase in β occurs and less atmospheric drag is experienced by the vehicle. This produces the discontinuity seen in the deceleration plot.
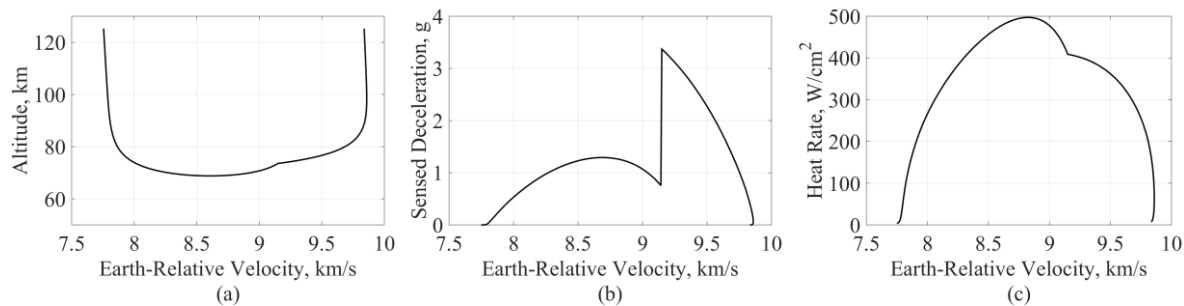

Figure 4. Nominal aerocapture trajectory: (a) altitude, (b) sensed deceleration, and (c) stagnation point heat rate versus Earth-relative velocity.

B. Uncertainty Analysis

An end-to-end Monte Carlo analysis was run to examine the robustness of the proposed spacecraft design and trajectory to uncertainty. This analysis considered sources of error throughout the spacecraft's entire trajectory to determine potential variation from the desired final orbit. Uncertainties were introduced at three distinct points: the PLM, the atmospheric portion of the aerocapture maneuver, and the PRM. The uncertainty sources considered and their values are shown in Table 3.

Table 3.   End-to-end Monte Carlo simulation uncertainty sources.

Trajectory Phase	Parameter	Dispersion
Perigee-lower maneuver	Initial GTO perigee	± 2 km
	Initial GTO apogee	± 10 km
	Coast time	± 300 s
	Burn ΔV	± 1.17%
Atmospheric flight	Atmospheric density & wind variations	Earth-GRAM
Perigee-raise maneuver	Coast time	± 300 s
	Burn ΔV	± 1.06%

The state errors from each distinct trajectory phase were propagated forward and considered as a source of error for subsequent phases. PLM and PRM coast times are a measurement of time until each burn is performed, from rideshare separation and atmospheric exit respectively. Burn ΔV dispersions were determined from manufacturer specifications for the proposed propulsion system, using IMU measurements as a cutoff value. Atmospheric uncertainties were obtained using the Global Reference Atmospheric Model for Earth, Earth-GRAM 2010[11]. The PLM burn magnitude is the driving source of uncertainty for this end-to-end simulation, as small variations can have a large effect on the flight path angle at atmospheric interface.

American Institute of Aeronautics and Astronautics

Table 4 shows the results of this Monte Carlo simulation. 10,000 samples were run, with a target final apogee altitude of 1,760 km and final perigee altitude of 180 km. The mean apogee and perigee are close to the desired values, signifying that the guidance algorithm is able to target the final orbit with a reasonable degree of accuracy. Histogram plots of the results are shown in Fig. 5. The bimodal distribution shown in the apogee histogram is a byproduct of the vehicle's sensitivity to the jettison event; small delays in jettison time can decrease the final apogee altitude by tens of kilometers. Increasing

Table 4.   End-to-end Monte Carlo simulation results.

Apsis	Parameter	Value
Apogee	Mean	1693.7 km
	3σ	169.5 km
	Minimum	1556.5 km
	Maximum	1766.7 km
Perigee	Mean	180.3 km
	3σ	4.8 km
	Minimum	174.1 km
	Maximum	188.3 km

the guidance execution rate is one way to help mitigate this effect. As modeled, the final apogee has a range of 210.2 km, while the final perigee range is 14.2 km. This level of accuracy is suitable for the purposes of this flight demonstration, although further guidance algorithm refinement may be required for future missions with more precise targeting requirements.
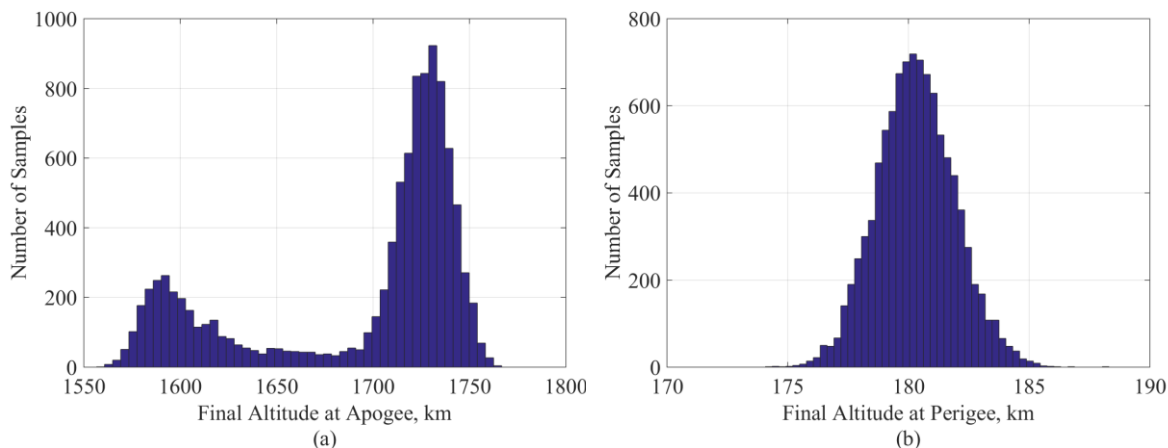

Figure 5. End-to-end Monte Carlo histograms: (a) final altitude at apogee, and (b) final altitude at perigee.

C. Relevance to Mars

A flight demonstration of aerocapture should have relevance to desired applications of the technique at different planetary targets. To this end, analogues can be drawn from the proposed Earth demonstration to orbital insertion at Mars, as the 2 km/s ΔV requirement is similar to that required for capture into a low Mars orbit. To assess the relevance of this mission concept to Martian aerocapture, trajectory and uncertainty analyses were carried out for an identical vehicle using single-event drag modulation to capture into orbit at Mars. For the purpose of these simulations, it is assumed that the smallsat is initially flying an eastbound equatorial trajectory, with initial conditions at atmospheric interface given in Table 5. The target orbit is identical to that of the Earth demonstration, with an apoapsis altitude of 1,760 km and a periapsis altitude of 180 km. Trajectory simulation results for nominal flight are shown in Fig. 6. Both the convective heat rate and peak deceleration are lower than those experienced during the proposed Earth flight test; therefore, a successful flight demonstration will validate an aerocapture system for environments more rigorous than what may be necessary for actual missions.

Table 5.   Mars trajectory simulation initial conditions.

Parameter	Value
Inertial velocity magnitude	6.0 km/s
Inertial flight path angle	-12°
Inertial azimuth	90°
Altitude	150 km
Latitude	0°
Longitude	0°

6

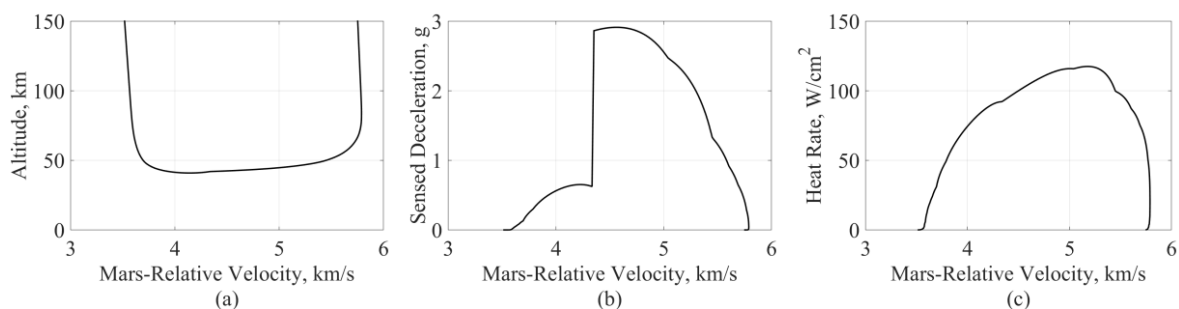American Institute of Aeronautics and Astronautics

Figure 6. Nominal Mars aerocapture trajectory: (a) altitude, (b) sensed deceleration, and (c) stagnation point heat rate versus Mars-relative velocity.

To assess uncertainty, a similar end-to-end Monte Carlo analysis was performed, featuring errors introduced at atmospheric interface and the subsequent PRM. State errors at atmospheric interface are based on MSL approach navigation results[12], and errors during the PRM were generated similarly to those for the Earth demonstration. These dispersions are listed in Table 6.

Table 6.   Mars end-to-end Monte Carlo simulation uncertainty sources.

Trajectory Phase	Parameter	Dispersion
Atmospheric interface & flight	Entry flight path angle	$\pm 0.013°$
	Atmospheric density & wind variations	Mars-GRAM
Perigee-raise maneuver	Coast time	± 300 s
	Burn ΔV	$\pm 1.08\%$

Results for a 10,000 sample Monte Carlo are shown in Table 7 and Fig. 7. The apoapsis histogram displays a similar bimodal distribution to the results from the Earth simulation. The apoapsis and periapsis ranges indicate that the spacecraft is able to capture into Mars orbit successfully, with some variation. Although greater precision is likely required for Mars science missions, an actual Mars aerocapture vehicle will be far less limited by rideshare constraints than the one considered for this study. Realistically, such a vehicle could feature a much larger change in β during drag modulation, which could lead to a more accurate final orbit.

Table 7.   Mars end-to-end Monte Carlo simulation results.

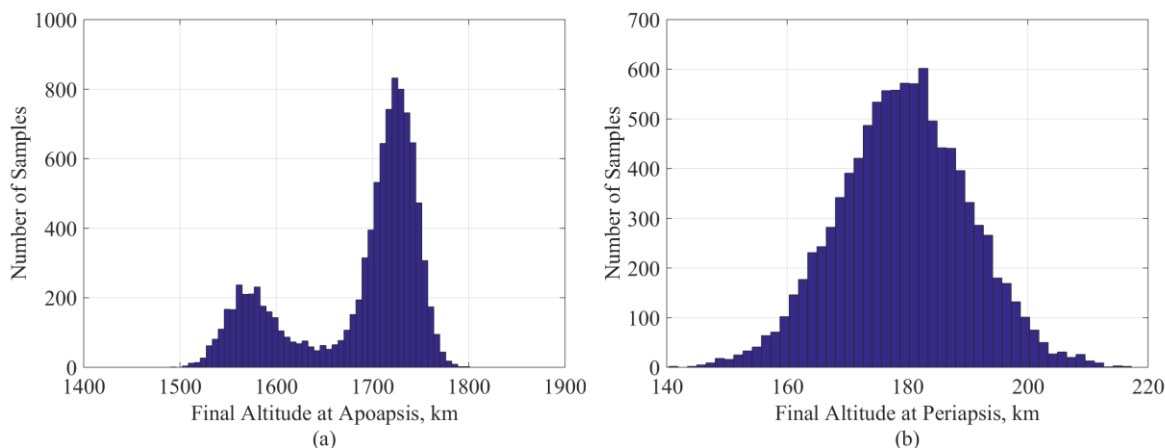| Apsis	Parameter	Value
Apoapsis	Mean	1685.0 km
	3σ	201.3 km
	Minimum	1490.0 km
	Maximum	1801.0 km
Periapsis	Mean	179.4 km
	3σ	32.5 km
	Minimum	140.4 km
	Maximum	217.2 km

7

American Institute of Aeronautics and Astronautics

Figure 7. Mars end-to-end Monte Carlo histograms: (a) final altitude at apoapsis, and (b) final altitude at periapsis.

IV. Mechanical Design

A. Aeroshell Design

The design of the spacecraft's aeroshell is directly intertwined with a number of mission aspects. Due to the extreme environments experienced during aerocapture, the aeroshell must be robust to large temperature ranges, vibrations, and structural loads. The geometry of the aeroshell is also restricted by launch vehicle requirements for rideshare volume; SSL specified a 1m x 0.5m x 0.4m volume available for secondary payloads, which places limits on the drag skirt outer radius and the longitudinal chord of the vehicle. The size of the drag skirt in relation to the main spacecraft body also directly impacts the β-ratio β_1/β_2 between the spacecraft's pre- and post-jettison configurations. As elaborated in Ref. 10, this ratio governs how much control authority can be imparted by drag modulation.

CAD files for the foreshell, backshell, and drag skirt are shown in Fig. 8, Fig. 9, and Fig. 10 respectively. Key design parameters for each of these features are listed in Table 8. A 60° sphere-cone design was selected due to the benefits it offers for heating, drag, and stability[13], and its use on prior small probe mission such as Genesis[14] and Stardust[15]. The selected nose and shoulder radii correspond to 9/16 and 1/16 of the foreshell outer radius, respectively, and were also based on heritage values from Genesis and Stardust.

The backshell was designed to accommodate a 2U rectangular prism payload, and features symmetric slots to enable deployment of the communications system's four orthogonal antennae. In order to mitigate internal heating concerns, the aft face of the backshell was left open. A conical taper was included such that the backshell is parallel to the foreshell shoulder at their interface. This design also helps mitigate static stability concerns and reduces drag following the jettison event.

The drag skirt structure was broken into four quadrants, to minimize machining constraints and help reduce the risk of re-impact after jettison. Both the outer and inner radii of the drag skirt were sized with the goal of maximizing the β-ratio between pre- and post-jettison configurations. As a result, the outer radius matches the largest possible dimension of the given rideshare constraint, with the inner

Table 8. Aeroshell design parameters.

Aeroshell Section	Parameter	Value
Foreshell	Radius	10 cm
	Nose radius	5.63 cm
	Shoulder radius	0.56 cm
	Longitudinal length	4.15 cm
	Sphere-cone half angle	60°
	Material thickness	0.3 cm
	Mass	0.27 kg
Backshell	Fore-end radius	10 cm
	Aft-end radius	7.5 cm
	Longitudinal length	21 cm
	Taper angle	5.3°
	Material thickness	0.3 cm
	Mass	0.91 kg
Drag skirt	Outer radius	25 cm
	Inner radius	10 cm
	Sphere-cone half angle	60°
	Material thickness	0.3 cm
	Mass	1.64 kg
Total	Mass	2.82 kg
	Length	25.15 cm
	Outer radius	25 cm

8

American Institute of Aeronautics and Astronautics

radius driven by backshell size. The foreshell, backshell, and drag skirt are all made of 3mm thick 6061 aluminum to facilitate prototyping and machining at a university scale.

(a)   (b)

Figure 8. Foreshell CAD views: (a) front isometric, and (b) rear isometric.
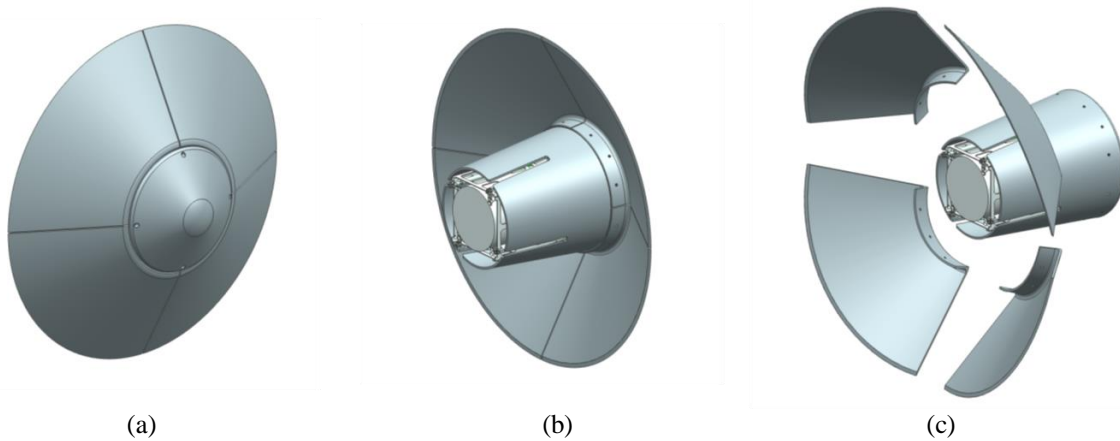

(a)   (b)

Figure 9. Backshell CAD views: (a) front isometric, and (b) side.

(a)   (b)   (c)

Figure 10.   Drag skirt CAD views: (a) front isometric, (b) rear isometric, and (c) post-jettison rear isometric.

9

American Institute of Aeronautics and Astronautics

B. Stability and Heating Analysis

To assess the stability characteristics of the spacecraft before and after jettison, a first order CG estimate and CFD analysis of the system was conducted using CBAero, a software tool that uses accepted engineering analysis for the approximation of aerodynamic environments[16]. This analysis produced $C_{m,\alpha}$ and $\hat{x}$ values for discretized points in the spacecraft's nominal trajectory. The results, shown in Table 9, reveal a very wide $\hat{x}$ pre-jettison and smaller (yet still stable) values post-jettison for the atmospheric regime of interest. The negative $\hat{x}$ values following atmospheric egress are believed to be caused by the very low Knudsen numbers in this flight regime, and may not be cause for concern as a result. With regards to the dynamic stability of the system, it was estimated that the highly-hypersonic, high altitude and correspondingly low density flow flight regime will cause the vehicle to remain in an oscillatory stable configuration throughout its atmospheric trajectory.

Aerocapture, much like other EDL methods, can result in severe aerothermodynamic environments. For this demonstration, phenolic impregnated carbon ablator (PICA) was selected as spacecraft's thermal protection system (TPS) material due to its availability and ability to withstand the high heat rates generated during the aerocapture maneuver. A first-order TPS sizing estimate was generated based on the peak stagnation point heat rate produced by the trajectory model; this analysis resulted in a baseline 4.2 cm thick layer of PICA applied to the entire spacecraft.

Table 9. Pre- and post-jettison static margin values.

Configuration	Time (s)	$\hat{x}$ (cm)
Pre-jettison	0	N/A
	50	63.42
	100	58.99
	150	58.64
Post-jettison	200	7.98
	250	8.52
	300	11.34
	350	-3.31
	400	-243.88
	450	N/A

During the design process, it was noted that this baseline value is a conservative estimate, as most of the vehicle will not experience heat rates as high as those at the stagnation point. In order to investigate the possibility of TPS mass reductions, previous experimental and theoretical heating results (detailed in Ref. 17) were used to generate discretized heat rates along the forward flank of the aeroshell, as well as the backshell. It was found that heat flux values along the conical frustum could be approximated as 45% to 65% of those seen by the stagnation point, and values along the backshell were approximately 10% of the stagnation point heat flux. These new approximate heat rates were used to generate a second TPS sizing estimate, featuring distinct thicknesses of PICA applied to different locations along the vehicle. The updated sizing estimate is shown in Table 10.

Table 10. Discretized TPS sizing values.

Location	PICA Thickness (cm)
Foreshell nose	4.2
Foreshell flank and drag skirt	4
Backshell	3.5

C. Drag Skirt Structural Analysis and Jettison Mechanism

As the primary source of deceleration for the spacecraft, the attached rigid drag skirt must be capable of withstanding potentially large structural loads. To analyze the performance of the selected design in response to peak loading conditions, an ANSYS structural analysis was run on both the individual drag skirt quadrants and on an assembly of all four quadrants. Static pressure loading on the drag skirt was determined from dynamic and freestream pressure values throughout the spacecraft's pre-jettison trajectory. A pressure of 6.4 kPa was applied to each quadrant and to the complete drag skirt assembly, with the base of each quadrant fixed as a boundary condition. The results, shown in Fig. 11 – 14, indicate that the stresses in each section are well below the critical yielding stress of machined 6061 aluminum (~270 MPa).
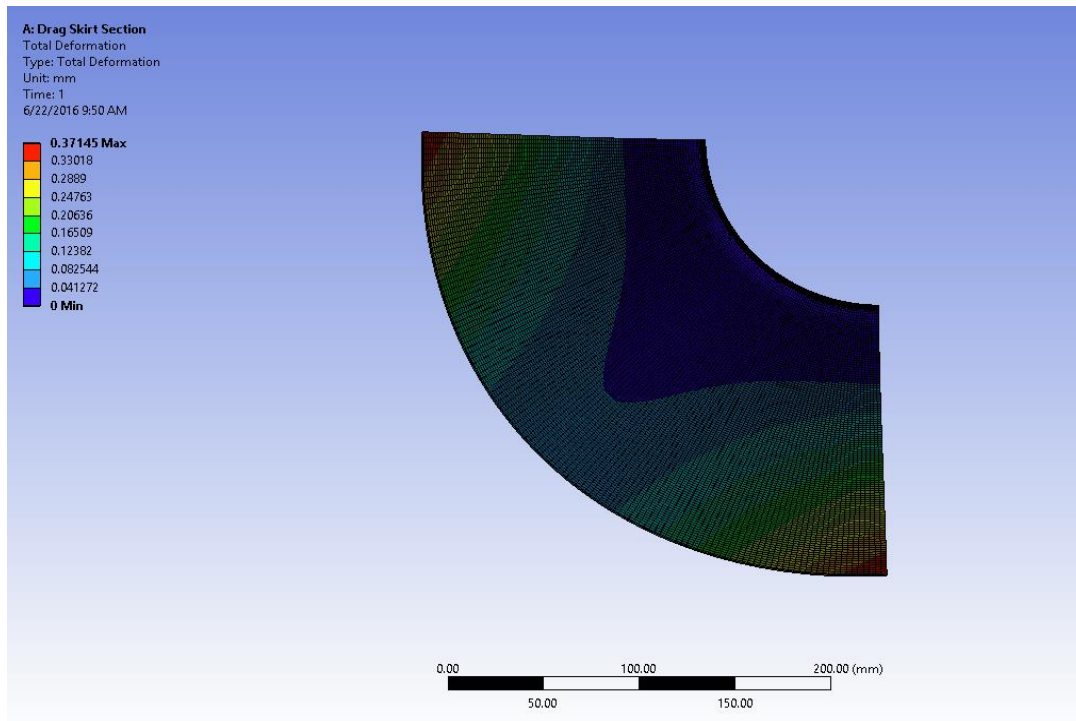
American Institute of Aeronautics and Astronautics

Figure 11.   Single quadrant deflection analysis.
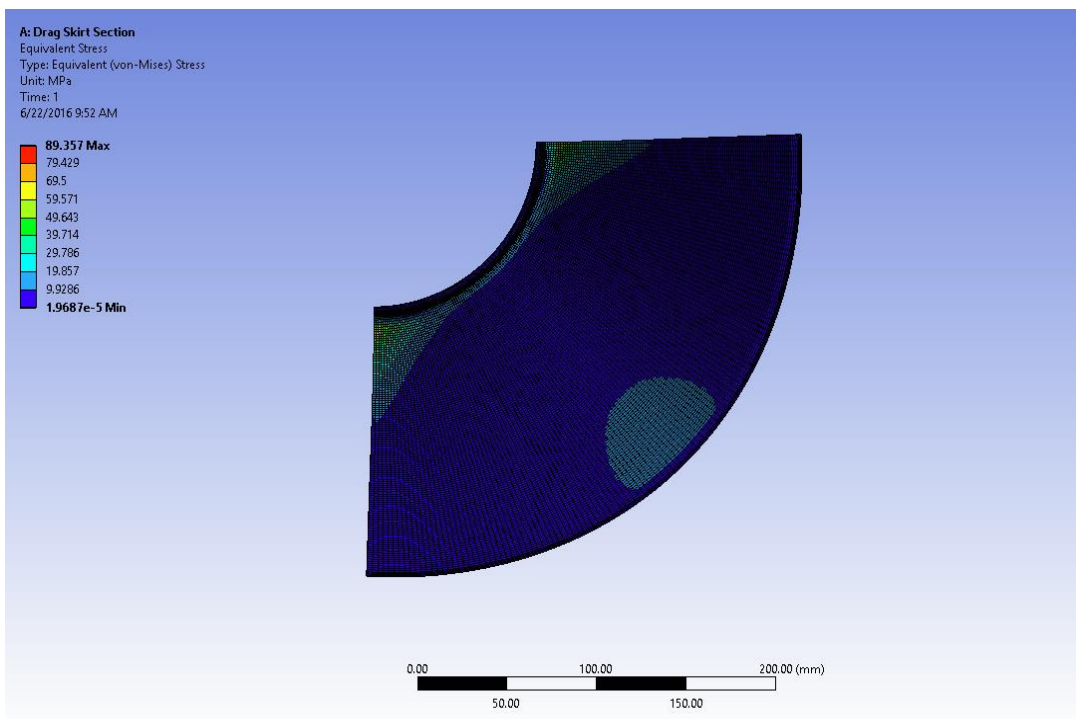
Figure 12.   Single quadrant von Mises stress analysis.
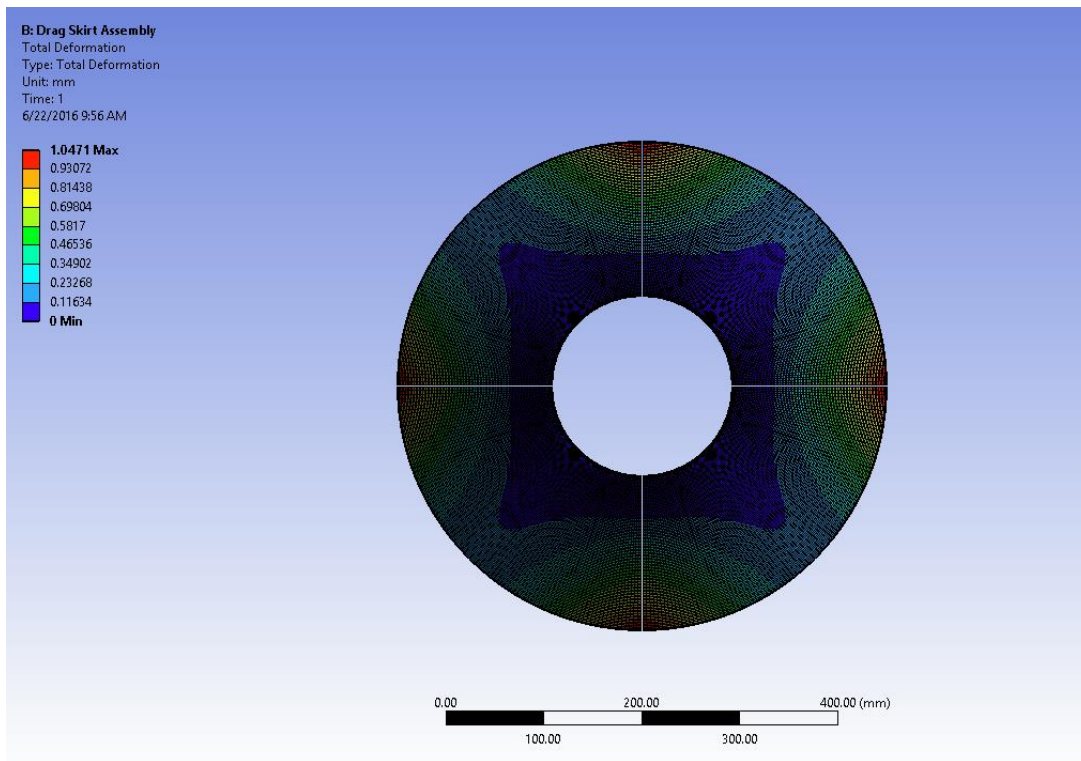
American Institute of Aeronautics and Astronautics

Figure 13.   Drag skirt assembly deflection analysis.
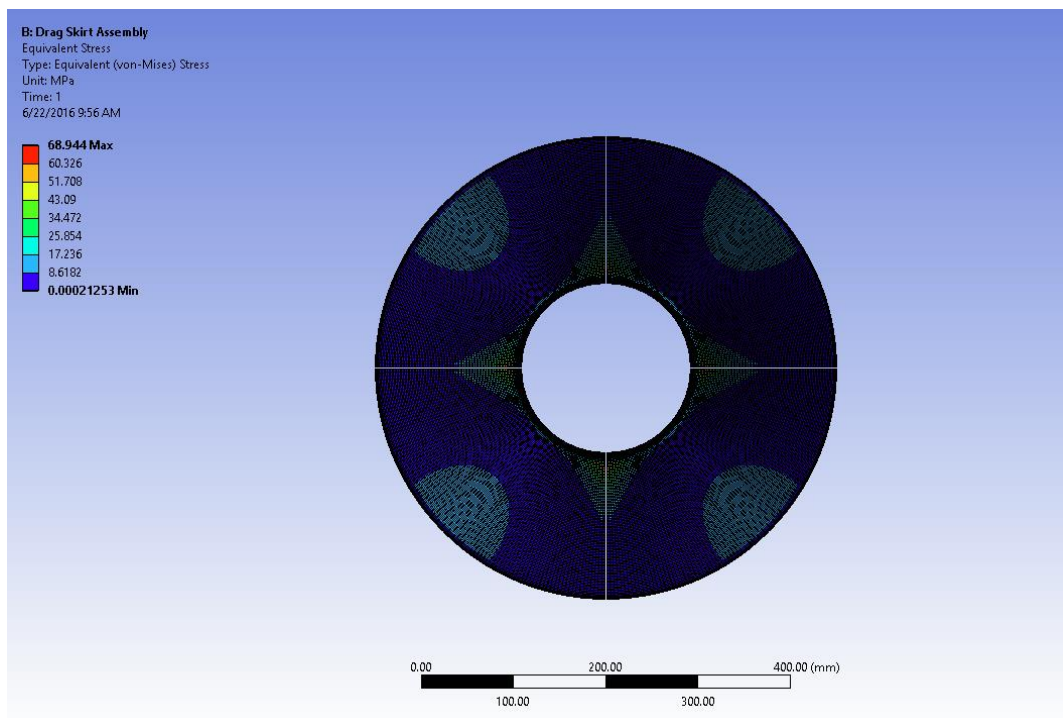
Figure 14.   Drag skirt assembly von Mises stress analysis.

12
American Institute of Aeronautics and Astronautics

Each drag skirt quadrant is attached to the backshell using 3 pyrotechnic NASA Standard Initiator (NSI) M3 break bolts, which have been used on a number of prior NASA missions. When the jettison event is triggered, these bolts are detonated, causing the quadrants to separate from the backshell. A shear loading analysis was performed on the bolts, and the results indicate that the peak stresses experienced are far below specified material yielding properties.

One key risk regarding the jettison event is the potential for re-impact between the drag skirt and the spacecraft. To help allay this concern, a first-order dynamics analysis was performed to determine the smallsat's sensitivity to recontact with the drag skirt components. The $C_{m,\alpha}$ of the post-jettison vehicle was plotted as a function of α in order to determine the point at which instability is reached. This plot, shown in Fig. 15, indicates that the vehicle could safely withstand a perturbation α of approximately 57.5° before becoming statically unstable. Upon exceeding this critical value of α, the vehicle would rotate unstably about the y-axis before returning to potential stable configurations (-57.5° $\lesssim \alpha \lesssim$ 57.5°). These results are promising indications that drag-skirt re-impact may not result in mission failure.
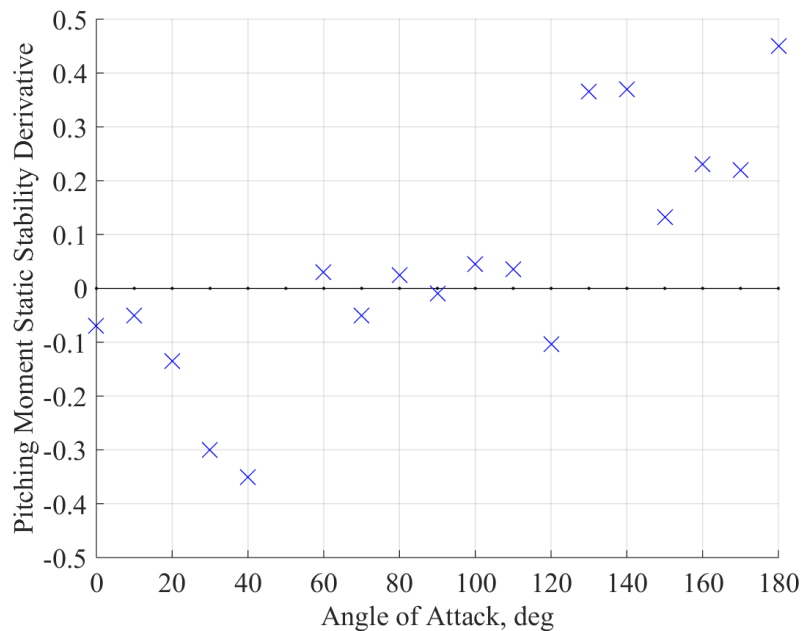

Figure 15.   Post-jettison vehicle pitching stability.

D. Interface with Host

The Planetary Systems Corporation Mark II Motorized Lightband was selected as interfacing hardware to control the aerocapture vehicle's separation from its host spacecraft, due to its commercial availability and heritage for CubeSat and smallsat missions. Figure 16 displays the interface between the Lightband and the aeroshell. The Lightband is attached to the backshell via four orthogonally-spaced L-brackets, with pyrotechnic NSI M3 bolts used as fasteners. Similar to the drag skirt jettison mechanism, these bolts will fire exo-atmospherically after the PLM, such that the Lightband and L-brackets are separated from the entry vehicle prior to aerocapture.
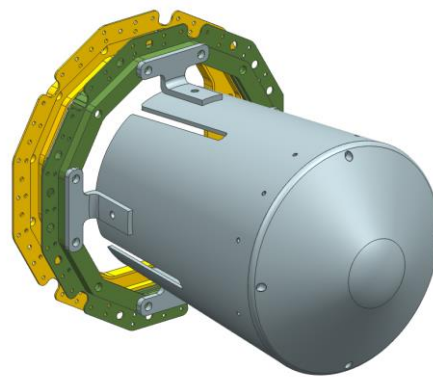

Figure 16.   8" Lightband interface with backshell.

13

American Institute of Aeronautics and Astronautics

V. Flight System Design

In keeping with the design philosophy used for other aspects of this mission, the design of the flight system prioritized simple and functional hardware. A flight system consisting primarily of commercially available, off-the-shelf components can be feasibly constructed at a university scale, with a minimal budget when compared to more complex demonstrations. Table 11 contains a mass summary of the proposed design, including current best estimates (CBE), contingency, and maximum expected values (MEV). Subsystem requirements were generated in part by a concurrent design study through the Team-Xc program at NASA JPL, which enabled comprehensive iterations through different design choices. The total hosted mass of the spacecraft with contingency added is 24.9 kg, which falls well within the range of secondary payload requirements.

Table 11. Flight system mass summary.

Mass Summary	CBE	Contingency	MEV
	kg	%	kg
Flight System	**15.4**	**21%**	**18.7**
Spacecraft Bus	**7.8**	**12%**	**8.8**
Power	1.2	30%	1.6
C&DH	0.2	30%	0.2
Telecom	0.1	14%	0.1
Structure	0.7	30%	0.9
Thermal	4.2	0%	4.2
Propulsion	0.6	30%	0.8
GN&C	0.1	5%	0.1
Cabling	0.7	15%	0.8
Aeroshell	**7.6**	**30%**	**9.9**
Margin			**18%**
JPL Mass Margin			30%
JPL Margined Dry Mass			**22.1**
Total Propellant			**0.74**
Propellant			0.74
Spacecraft-side Separation System			0.51
Spacecraft Mass – Fully Margined			**23.3**
ComSat-side Separation System			1.62
Total Hosted Mass			**24.9**

Figure 17 shows an overview of the flight system and its placement within the aeroshell. The proposed component placement helps to drive the CG of the spacecraft forward, and enables the use of the propulsion system, foreshell, and backshell as heat sinks for the remaining internal components. Due to the lack of radiator space available within the backshell, an additional 4.2 kg mass of aluminum is placed towards the nose of the spacecraft to serve as a heat sink and structural support for the flight system components.
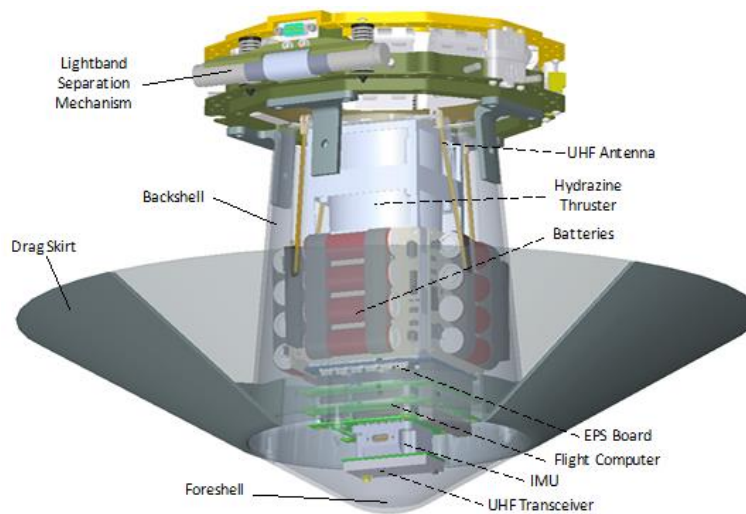

Figure 17.   Key flight system components.

14

American Institute of Aeronautics and Astronautics

A summary of the power budget for the spacecraft's operations is given in Table 12. Power is allocated for up to 6 downlink passes over the continental US following the aerocapture maneuver, which will provide adequate margin for the selected UHF communication system to downlink the data products required by the proposed mission success criteria for up to one day.

Table 12. Power budget summary.

Power Modes Summary	Mode Duration (hr)	CBE Power (W)	Contingency (%)	MEV Max Expected Power (W)	MEV Energy Required per Mode (W-hr)	MEV Cumulative Energy Required (W-hr)
Warmup	0.17	7.8	15.0	8.9	1.5	1.5
Cruise 0	0.83	7.8	15.0	8.9	7.5	8.9
PLM ΔV	0.02	4.0	15.0	4.6	0.1	9.0
Telecom 1	0.05	22.2	15.0	25.6	1.3	10.3
Cruise 1	5.19	7.8	15.0	8.9	46.4	56.7
Aerocapture	0.11	9.2	15.0	10.6	1.2	57.9
Cruise 2 & Flip	0.88	9.2	15.0	10.6	9.4	67.3
PRM ΔV	0.05	4.0	15.0	4.6	0.2	67.5
Cruise 3	23.32	0.8	15.0	0.9	21.3	88.8
Downlink	1.67	13.8	15.0	15.9	26.4	115.2
Total	**32.28**					**115.2**

VI.   Conclusion

A comprehensive mission concept for an Earth-based flight demonstration of drag-modulated aerocapture has been developed. The proposed concept would help to validate the use of aerocapture, provide data products from the maneuver, and has relevance to missions at Mars and other targets. Trajectory and uncertainty analyses show the feasibility of the proposed trajectory, and demonstrate its robustness to day-of-flight uncertainties. Mechanical and systems evaluations show that a 24.9 kg spacecraft featuring commercially-available components can survive the rigors of an aerocapture maneuver.

Future developmental work for this mission concept may include development of a mechanism to enable spinning separation from the host spacecraft, further investigation into the static and dynamic stability characteristics of the vehicle, higher-fidelity analysis of the drag skirt jettison event and exploration of the guidance algorithm trade space. In-depth modeling of the drag skirt jettison event can help minimize the risks of recontact. Additional guidance algorithm investigation and development may result in a more computationally efficient drag modulation algorithm for the degree of accuracy required for this demonstration.

Acknowledgments

References

[1]Walberg, G. D., "A Survey of Aeroassisted Orbit Transfer," *Journal of Spacecraft and Rockets*, Vol. 22, No. 1, 1985, pp. 3-18.

[2]Hall, J. L., Noca, M. A., and Bailey, R. W., "Cost-Benefit Analysis of the Aerocapture Mission Set," *Journal of Spacecraft and Rockets*, Vol. 42, No. 2, 2005, pp. 309-320.

American Institute of Aeronautics and Astronautics

[3]Miller, K. L., Gulick, D., Lewis, J., Trochman, B., Stein, J., Lyons, D. T., and Wilmoth, R. G., "Trailing Ballute Aerocapture: Concept and Feasibility Assessment," *39th AIAA/ASME/SAE/ASEE Joint Propulsion Conference and Exhibit*, Huntsville, AL, July 2003.

[4]Lockwood, M. K., "Titan Aerocapture Systems Analysis," *39th AIAA/ASME/SAE/ASEE Joint Propulsion Conference and Exhibit,* Huntsville, AL, July 2003.

[5]Lockwood, M. K., "Neptune Aerocapture Systems Analysis," *AIAA Atmospheric Flight Mechanics Conference and Exhibit*, Providence, RI, August 2004.

[6]Hall, J. L., "An Overview of the ST-7 Aerocapture Flight Test Experiment," *AIAA Atmospheric Flight Mechanics Conference and Exhibit*, Monterey, CA, August 2002.

[7]McRonald, A., "A Light-Weight Inflatable Hypersonic Drag Device for Planetary Entry," *Association Aeronautique de France Conference*, Arcachon, France, March 1999.

[8]Lyons, D. T., and Johnson, W. R., "Ballute Aerocapture Trajectories at Neptune," *AIAA Atmospheric Flight Mechanics Conference and Exhibit*, Providence, RI, August 2004.

[9]Putnam, Z. R., Clark, I. G., and Braun, R. D., "Drag Modulation Flight Control for Aerocapture," *Aerospace Conference, 2012 IEEE*, Big Sky, MT, March 2012, pp. 1-10.

[10]Putnam, Z. R., and Braun, R. D., "Drag Modulation Flight Control System Options for Planetary Aerocapture," *Journal of Spacecraft and Rockets*, Vol. 51, No. 1, 2014, pp. 139-150.

[11]Leslie, F. W., and Justus, C. G., "The NASA Marshall Space Flight Center Earth Global Reference Atmospheric Model-2010 Version," NASA/TM-2011-216467, June 2011.

[12]Martin-Mur, T. J., Kruizinga, G. L., and Wong, M. C., "Mars Science Laboratory Interplanetary Navigation Analysis," *22nd International Symposium on Space Flight Dynamics*, São José dos Campos, Brazil, March 2011.

[13]Mitcheltree, R. A., Moss, J. N., Cheatwood, F. M., Greene, F. A., and Braun, R. D., "Aerodynamics of the Mars Microprobe Entry Vehicles," *Journal of Spacecraft and Rockets*, Vol. 36, No. 3, 1999, pp. 392-398.

[14]Cheatwood, F. M., Merski, N. R., Jr., Riley, C. J., and Mitcheltree, R. A., "Aerothermodynamic Environment Definition for the Genesis Sample Return Capsule," *35th AIAA Thermophysics Conference*, Anaheim, CA, June 2001.

[15]Mitcheltree, R. A., Wilmoth, R. G., Cheatwood, F. M., Brauckmann, G. J., and Greene, F. A., "Aerodynamics of Stardust Sample Return Capsule," *Journal of Spacecraft and Rockets*, Vol. 36, No. 3, 1999, pp. 429-435.

[16]Kinney, D. J., "Aero-Thermodynamics for Conceptual Design," *42nd AIAA Aerospace Sciences Meeting and Exhibit*, Reno, NV, January 2004.

[17]Woollard, B. A., and Braun, R. D., "Mechanical Design of a Cubesat Aeroshell for an Earth Demonstration of Single-Stage Drag Modulated Aerocapture," SSDL Masters Projects, Georgia Institute of Technology, Atlanta, GA, 2016 (unpublished).

American Institute of Aeronautics and Astronautics